CRYSTAL GROWTH & DESIGN
2009
VOL. 9, NO. 4
1793–1797

Interfacial Diffusion during Growth of SnO_2(110) on TiO_2(110) by Oxygen Plasma Assisted Molecular Beam Epitaxy

Robert G. Palgrave, Anne Bourlange, David J. Payne, John S. Foord, and Russell G. Egdell*

Chemistry Research Laboratory, University of Oxford, 20 Mansfield Road, Oxford, OX1 3TA United Kingdom

Received August 26, 2008; Revised Manuscript Received December 22, 2008

ABSTRACT: Oxygen plasma-assisted molecular beam epitaxy was used to grow layers of SnO_2 on single-crystal rutile TiO_2 (110) substrates. Surface composition was studied by X-ray photoelectron spectroscopy, whereas secondary ion mass spectrometry was used to determine the depth distribution of Sn and Ti. For substrate temperatures below 600 °C, SnO_2 grows as an epitaxial film on top of the TiO_2, but at higher temperatures there is evidence for pronounced interdiffusion between the substrate and the epilayer. At growth temperatures above 775 °C the Sn diffuses rapidly into the substrate to give Sn-doped TiO_2 rather than a distinct SnO_2 epilayer. The films were all highly (110) oriented but the lattice parameter of the deposited film decreased with increasing growth temperature, consistent with the formation of $Ti_xSn_{1-x}O_2$ solid solutions through interfacial solid-state reaction in a narrow temperature regime between 750 and 775 °C.

Introduction

SnO_2/TiO_2 is an intriguing mixed-oxide system that has been extensively studied and linked with a number of applications. SnO_2 and TiO_2 share similarities in electronic and crystal structure: both are wide band gap n-type semiconductors, and both crystallize in the tetragonal rutile crystal system. The lattice parameters for SnO_2 are however somewhat larger than those for TiO_2. Above 1450 °C, TiO_2 and SnO_2 form thermodynamically stable solid solutions of formula $Ti_xSn_{1-x}O_2$ across the whole composition range $0 \leq x \leq 1$. The phase diagram for SnO_2/TiO_2 has been determined down to 500 °C,[1] and indicates a nearly symmetrical miscibility gap, with stable Sn-rich ($x < 0.15$) and Ti-rich ($x > 0.85$) phases at temperatures below 900 °C.

The SnO_2/TiO_2 system has been investigated for a number of possible applications. SnO_2 is a prototype gas sensing material, which changes its resistivity in response to the interaction of oxidising or reducing gases with the oxide surface.[2,3] However, the limited long-term stability of SnO_2 at the high operating temperatures required for gas sensing is a concern. In an effort to improve stability, and the selectivity of the SnO_2 surface to different gases, Ti-doped SnO_2 sensors have been investigated by several groups.[4−7] Another promising application of Sn-doped TiO_2 is in visible light photocatalysis.[4−12] For both of these areas of application, the study of well-defined samples produced by molecular beam epitaxy (MBE) offers the promise of furthering understanding of the fundamental surface physics of this complex system.[13] One aspect of particular importance is the differentiation of electronic structure and functional properties between heterostructures involving an SnO_2/TiO_2 interface and solid solutions phases of the sort $Ti_xSn_{1-x}O_2$.[7]

Epitaxial films of SnO_2 have been grown on various crystal faces of rutile TiO_2 by sputtering,[14] pulsed laser deposition[15] and chemical vapour deposition,[16] and on sapphire by MBE.[17] The motivation in several of these studies has been the creation of ideal surfaces for investigation of functional properties, especially gas sensing.[14] There is significant lattice mismatch between TiO_2 and SnO_2 which might be expected to hinder epitaxial growth; in the *a* direction the lattice mismatch is $(a_{SnO_2} - a_{TiO_2})/a_{TiO_2} = (473\text{ pm} - 461\text{ pm})/461\text{ pm} = +2.6\%$, whereas in the *c* direction, the mismatch is $(c_{SnO_2} - c_{TiO_2})/c_{TiO_2} = (320\text{ pm} - 297\text{ pm})/297\text{ pm} = +7.7\%$.[18] Diebold et al. suggested that the lattice mismatch might be overcome through diffusion of Sn and Ti between the growing film and substrate, forming a solid solution at the interface.[18] This solid solution might lead to a gradual change in lattice parameters, relieving strain and promoting epitaxial growth. The use of interdiffusion to produce epitaxial $Ti_xSn_{1-x}O_2$ films would also be of interest. However, such diffusion has not been previously observed experimentally. In this paper, we report an investigation into the SnO_2/TiO_2 interface in epitaxial films grown using oxygen plasma assisted molecular beam epitaxy, provide direct evidence of interfacial metal ion diffusion, and quantify the diffusion by calculating the diffusion coefficients for each metal cation.

Experimental Section

Tin oxide layers were grown on rutile TiO_2 (110) substrates supplied by Pikem Ltd. in a UHV oxide MBE system (SVT, Eden Prairie, MN) with a base pressure of 5×10^{-10} mbar. This incorporated a conventional Sn Knudsen cell and a radio frequency oxygen plasma atom source operated at 200 mW rf power with an oxygen background pressure of 5×10^{-5} mbar. The Sn Knudsen cell was heated to 1120°C, and the nominal metal deposition rate was set at 0.01 nm s^{-1} using a quartz crystal monitor offset from the sample position. Substrates were cleaned by treating ultrasonically in acetone followed by propan-2-ol for 10 min. After introduction to UHV, the substrates were heated radiatively using a graphite filament to the desired growth temperature, T_g, which was varied between 500 and 900 °C. After the required temperature was attained, substrates were exposed to the oxygen plasma beam for 5 minas a final cleaning step and to ensure oxidation of the surface prior to film growth. Films were then grown by exposing the substrate simultaneously to the Sn and O beams for 50 minutes. The substrate was cooled in the presence of the O atom beam. Low energy electron diffraction was carried out in situ in an analysis chamber connected to the growth chamber. High-resolution X-ray photoemission spectra (XPS) were recorded in a Scienta ESCA 300 spectrometer located at Daresbury Laboratory, UK, which incorporated a rotating anode Al K_α ($h\nu$ =1486.6 eV) X-ray source. The X-ray source was run with 200 mA emission current and 14 kV anode bias, whereas the analyzer operated at 150 eV pass energy with 0.8 mm slits. Gaussian convolution of the analyzer resolution with a linewidth of 260 meV

* Corresponding author. E-mail: Russell.egdell@chem.ox.ac.uk

10.1021/cg8009404 CCC: $40.75 © 2009 American Chemical Society
Published on Web 02/13/2009

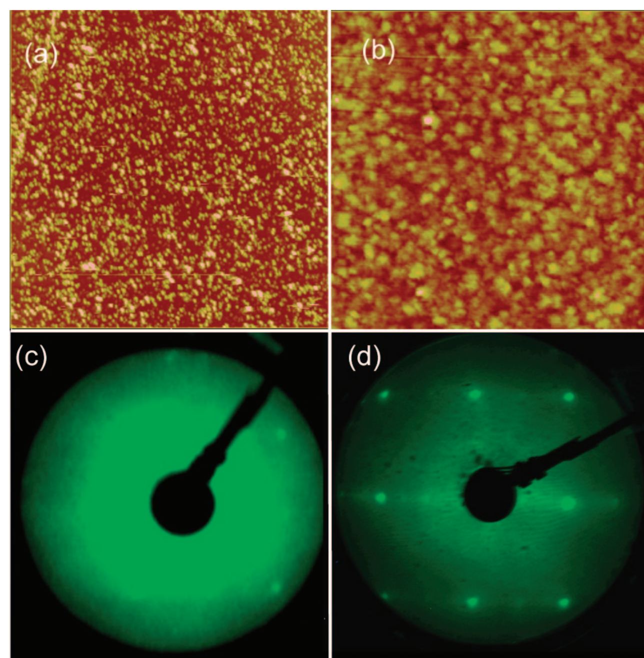

Figure 1. (a) 5 μm × 5μm AFM image of film grown at 500 °C. The colour scale in the image extends over 100 nm and the rms roughness is 8.7 nm. (b) 5 μm × 5μm AFM image of film grown at 750 °C. The colour scale in the image extends over 10 nm and the rms roughness is 0.7 nm. (c) LEED pattern from film grown at 500 °C, electron energy 115 eV. (d) LEED pattern from uncoated TiO_2 (110) substrate, electron energy 88 eV.

for the monochromated X-ray source gives an effective instrument resolution of 450 meV. Powder X-ray Diffraction (XRD) was carried out on a Panalytical instrument using monochromated Cu $K_{\alpha 1}$ radiation. Secondary ion mass spectrometry (SIMS) was carried out using an Cameca IMS 3f SIMS instrument located at Loughborough Surface Analysis Ltd. A 10 kV O_2^- beam was used, with the sample held at 4.5 kV. Samples were sputter-coated with gold in order to reduce charging. After SIMS analysis the crater depths were measured with a Dektak 6M profilometer in order to produce a depth scale. AFM images were recorded in a Digital Instruments Multimode SPM instrument with a Nanoscope IIIa controller. This was operated in contact mode using silicon nitride tips with a scanner having a lateral range of approximately 100 μm and a vertical range of 6 μm.

Results

Film Morphology and Crystalline Order. AFM images of films grown at 500 °C and 750 °C are shown in Figure 1. The film grown at the lower temperature has a rough granular structure with a root mean square (rms) roughness of 8.7 nm and overall *z* displacement range of 100 nm in the 5 μm × 5 μm image. Nonetheless there is sufficiently good epitaxial registry with the substrate that well-defined low energy electron diffraction patterns are observed even from this macroscopically rough film; Figure 1 shows LEED patterns taken from the film grown at T_g = 500 °C, electron energy 115 eV (c) and the uncoated substrate, annealed at 500 °C in ultrahigh vacuum in the presence of the RF oxygen plasma beam with electron energy of 88.0 eV (d). Well-ordered growth is further confirmed by X-ray diffraction data to be discussed below. The film grown at 750 °C is much smoother with an rms roughness of only 0.8 nm and an overall *z* range of 10 nm in a 5 μm × 5 μm image.

X-ray Photoelectron Spectroscopy. XPS revealed a changing surface composition with increasing growth temperature; Figure 2 shows the Sn 3d and Ti 2p regions of the photoelectron spectrum taken from samples grown at different T_g.

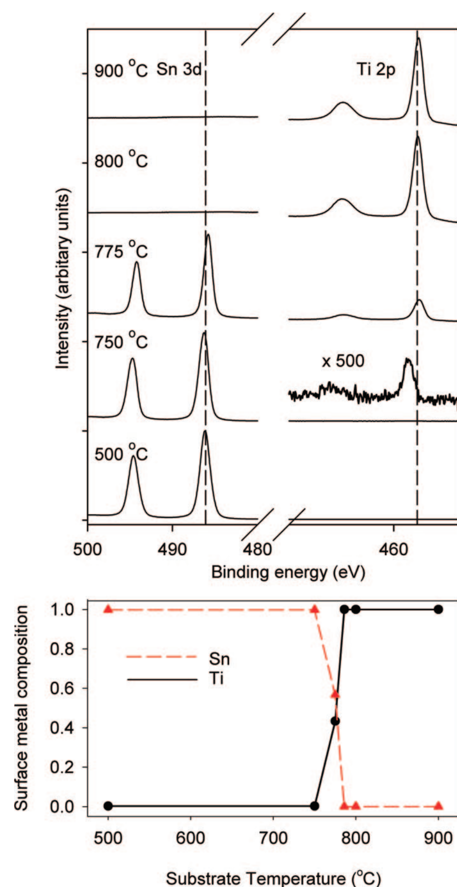

Figure 2. X-ray photoelectron spectra of samples grown at the temperatures indicated showing Sn 3d and Ti 2p core lines. The dashed lines represent the binding energy expected for the Sn $3d_{5/2}$ (higher binding energy) and the Ti $2p_{3/2}$ (lower binding energy) core lines of SnO_2 and TiO_2, respectively.

The presence of Sn, O and low amounts of Ti was detected in samples grown at T_g = 500, 750 °C. The Sn:Ti ratio in these films, calculated from the area of the 3d and 2p core lines, respectively, was approximately 500:1, and in both samples the Sn $3d_{5/2}$ core line binding energy was 486.3 eV, in agreement with previous studies of SnO_2.[18] The sample grown at T_g = 775 °C had a mixed composition, with a Sn:Ti ratio of 55:45. The Sn $3d_{5/2}$ core line was measured at 485.8 eV, shifted to lower binding energy by 0.5 eV compared with samples grown at lower temperatures, possibly indicating chemical interaction between Sn and Ti. The Ti $2p_{3/2}$ core line in this sample was observed with a principle component at 458.0 eV, which is consistent with Ti^{4+} in TiO_2,[19] in a 20:1 ratio with a weaker component at 456.5 eV, consistent with Ti^{3+} in sub-stoichiometric titanium dioxide.[20,21] The reduction of TiO_2 may have occurred at the elevated temperatures and low oxygen partial pressure during the MBE growth process. At higher T_g (800 and 900 °C), the surface appeared to be composed only of TiO_2; no Sn was detected within the sampling depth (approximately 50 Å) and detection limits (approximately 0.1 at %) of XPS. The Ti $2p_{3/2}$ core line in these samples appeared at a binding energy of 458.1 eV in each case, corresponding to Ti^{4+} in TiO_2.

X-ray Diffraction. Powder X-ray diffraction patterns taken in the range 2θ = 20−70° for the films grown at T_g = 500−775°C contained only peaks corresponding to the (110) and (220) Bragg reflections of rutile SnO_2 from the overlayer and rutile TiO_2 from the substrate (Figure 3). Each pattern has been adjusted to align the TiO_2 (110) peak with that of the

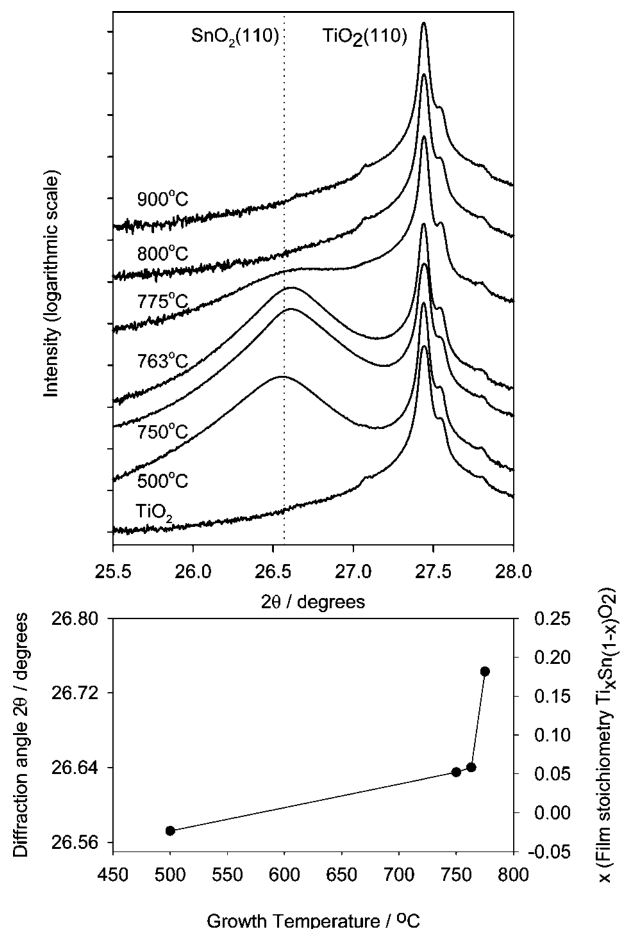

Figure 3. (Top) X-ray diffraction patterns for an untreated rutile TiO_2 (110) substrate and samples grown at T_g = 500-900 °C. In all samples, the TiO_2 (110) peak is present close to 27.5°. Some samples also show a SnO_2 (110) peak. The dashed line marks the expected position of the SnO_2 (110) peak. Bottom, stoichiometry of the Sn rich layer, calculated from the position of the SnO_2 (110) peak.

untreated substrate, the maximum that any pattern was adjusted in this way was ±0.02°. No peaks corresponding to anatase phase TiO_2 were observed. The absence of any other peaks indicates highly orientated epitaxial growth of the SnO_2 layer. XRD patterns for films grown at a higher temperatures (786 °C, 800 °C) contained only (110) and (220) TiO_2 peaks with no peaks corresponding to SnO_2. The sample grown at T_g = 775°C showed significantly weaker intensity SnO_2 (110) peak, possibly corresponding to a substantially thinner Sn rich layer. A closer look at the (110) Bragg reflection (Figure 3) shows deviation of the SnO_2 overlayer peaks to higher values of 2θ than for the pure SnO_2 phase, consistent with a contraction of the unit cell in the (110) direction caused by formation of a $Ti_xSn_{1-x}O_2$ solid solution. This deviation increases with T_g; the 2θ values of the SnO_2 (110) peak maxima in the T_g = 500, 750, 763, and 775 °C samples are 26.59, 26.64, 26.64, and 26.74°, respectively, a total variation of 0.13° across the samples.

The presence of diffraction peaks at 2θ values intermediate between those expected for SnO_2 and TiO_2 has been well-documented for $Ti_xSn_{1-x}O_2$ solid solutions across the entire composition range,[21] and thus diffraction results indicate that the layers grown by MBE might be best described as Sn-rich $Ti_xSn_{1-x}O_2$ solid solutions. The presence of so few diffraction peaks due to the highly crystallographically orientated nature of the samples makes Rietveld refinement of the patterns impossible, but the lattice parameter a of the tetragonal lattice can be calculated from the position of the (110) peaks. This is calculated as 4.740, 4.729, 4.728, and 4.710 Å for films grown at T_g = 500, 750, 763, and 775 °C, respectively. Hence, assuming a linear change in lattice parameters with changing solid solution composition (Vegard's law), the mean stoichiometry of the $Ti_xSn_{1-x}O_2$ overlayer probed in XRD can be calculated as x = 0, 0.05, 0.06, and 0.18, respectively. It should be noted that deviations from Vegard's law have been reported for the $Ti_xSn_{1-x}O_2$ system, as well as distortion of the tetragonal lattice such that the lattice parameter $a \neq b$,[21−23] which would introduce error into this calculation. However, these deviations are most prominent for $0.4 < x < 0.7$, i.e. near the middle of the solid solution composition range, within the miscibility gap, and are less-pronounced close to the end-members.[21] Similar systematic deviations in peak position of the TiO_2 (110) peak were not observed; this indicates that any Sn diffusion into the substrate is insufficient to alter the TiO_2 lattice parameter to an extent detectable by XRD; this is perhaps unsurprising considering the relative thickness of the substrate (approximately 1 mm) and the film (approximately 150 nm). Instead, the TiO_2 (110) peak position was constant to within 0.03°, and any variation within this range was not systematic with growth temperature, and is likely due to imperfect sample alignment, thus as stated previously, each diffraction pattern in Figure 3 was shifted to align the TiO_2 (110) peak with that of the untreated substrate at a 2θ value of 27.441°. Samples grown at T_g = 786 and 800 °C showed only a single set of (110) and (220) Bragg reflections at 2θ values, very close to those expected for rutile TiO_2 (Figure 2). The absence of a SnO_2 diffraction peaks indicates that no crystalline Sn-rich phase is present, and indeed, no Sn was detected on the surface of these samples by XPS.

Secondary Ion Mass Spectrometry (SIMS). SIMS was used to measure metal diffusion profiles. Figure 4 shows the SIMS profiles of samples grown in the range 500 °C < T_g < 800 °C. In concurrence with the XRD and XPS analyses, SIMS indicates that samples grown at T_g = 500−763 °C comprise a distinct Sn rich layer atop the TiO_2 substrate, where the Sn secondary ion signal is constant between 10^5 and 10^6 counts. Film thicknesses for these samples were determined by measuring the step height by profilometry from the uncoated region of the substrate (masked by the sample holder during the MBE growth) to the coated region. These heights ranged from 135−160 nm. After SIMS analysis, the crater depth was measured in the same way, and these two measurements were used create the depth scales used in Figure 4.

Looking in greater detail at the Sn profiles in panels a and b in Figure 4 it can be seen that at the lower growth temperatures (T_g = 500, 600 °C) the film−substrate interface is quite abrupt, with the Sn secondary ion signal intensity falling three orders of magnitude over a depth of 10 nm. There is, however, an extended weak tail, which indicates penetration of some Sn into the substrate. It should be considered this diffusion tail could result, at least in part, from mixing caused by the incident ion beam during the SIMS analysis. At growth temperatures of 750 and 763 °C, a more pronounced diffusion tail is evident, with Sn detectable at a sputtering depth of 300 nm, approximately 160 nm below the film-substrate interface. Figure 4b best illustrates the changing growth regime with increasing temperature. Unlike those samples grown at lower temperatures, samples grown at 775 and 800 °C display no distinct Sn-rich layer but simply a tail of Sn extending into the substrate from the surface. Figure 4c shows corresponding Ti depth profiles. At T_g = 500 and 600 °C, the interface between film and substrate is abrupt: the Ti secondary ion count diminishes to less than 1

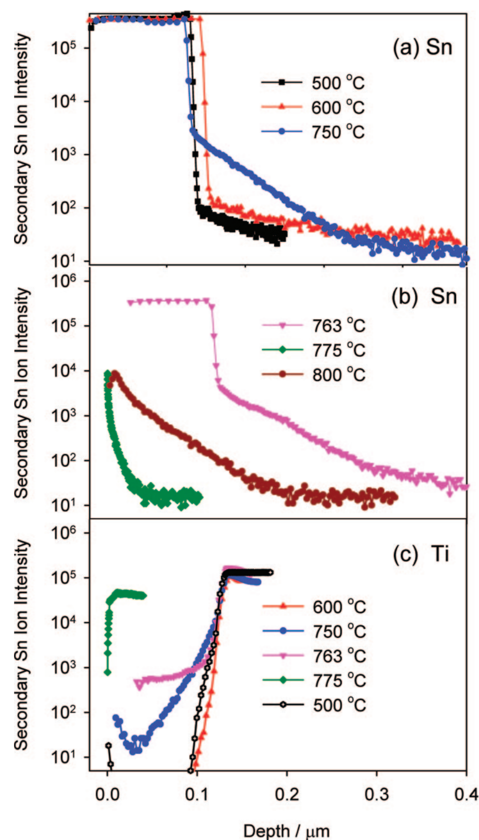

Figure 4. (a) SIMS Sn ion depth profiles of samples grown at 500, 600, and 750 °C. (b) SIMS Sn ion depth profiles of samples grown at 763, 775, and 800 °C. (c) SIMS Ti ion depth profiles showing diffusion of Ti into the Sn-rich layers. Distinct Sn rich layers can be discerned in samples grown at T_g = 763°C and below.

$\times$ 10^{-4} times its value in the TiO_2 substrate within 15 nm of the interface. It is again possible that mixing caused by the action of the incident ion beam has artificially increased this diffusion length, and the interface may in reality be more abrupt. Growth temperatures of 750 °C and 763 °C yielded much more extensive Ti diffusion tails, with Ti at detectable levels close to the upper surface of the film in each case. The absence of corresponding Ti signal in the XPS of these samples may be due to the lower sensitivity of XPS to trace elements compared with SIMS. The sample grown at T_g = 775 °C showed a quite different SIMS profile, with only a 10 nm Sn-rich layer, within which the Ti secondary ion signal dropped to approximately half of the value observed within the TiO_2 substrate. This is in broad accordance with the XPS analysis, which observed a Sn:Ti ratio of 55:45 at the surface of the sample. The SIMS data can also be compared with the XRD analysis. In the light of the SIMS data, the $Ti_xSn_{1-x}O_2$ compositions calculated from the XRD peak positions must be seen as mean compositions, because the composition of the Sn-rich overlayers changes throughout their thickness.

Discussion

From the analyses presented above, an explanation can be put forwards for the changing properties of the samples produced at different growth temperatures. If the film growth rate is greater than the rate at which Sn^{4+} diffuses into the substrate, then a Sn rich layer will form. In this case, there will be a discontinuity in the material composition at the interface between film and substrate. Conversely, if the diffusion rate is greater than the growth rate, i.e,. the incident Sn^{4+} ions diffuse into the substrate faster than they arrive, then a region of Sn doped TiO_2 will be present at the surface but no distinct Sn-rich layer will form and there will be no abrupt interface between film and substrate. A lower sticking probability of the incident Sn, expected at higher growth temperatures, would also disfavour formation of a Sn-rich layer. The cross over point between these two growth regimes has been determined as between T_g = 775 °C and T_g = 800 °C, although likely to be closer to the lower limit, as at this temperature only a 10 nm Sn-rich layer is formed.

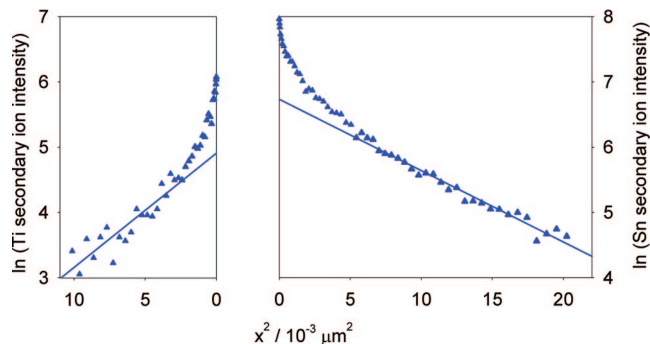

Figure 5. Plots of secondary ion yields of Ti and Sn as a function of square of displacement from SnO_2/TiO_2 interface for film grown at 750 °C.

Cation diffusion occurs through motion of point defects in the cation sublattice. It is well-established that the principle point defects in rutile TiO_2 at all temperatures and O_2 partial pressures are the O vacancy and the Ti interstitial.[24−26] However, in SnO_2, there is a significant concentration of intrinsic Sn vacancies.[27] Thus either the interstitial or vacancy diffusion mechanism could conceivably operate in the $Ti_xSn_{1-x}O_2$ materials studied here. Cation diffusion in the SnO_2/TiO_2 system has been studied by Drobeck et al. who inferred an interstitial diffusion mechanism involving tetravalent cation interstitial defects.[28] In their work, the addition of substitutional pentavalent cation dopants, expected to reduce the cation interstitial concentration, duly reduced the diffusion rate; further addition of the dopant caused an increase in rate, suspected to be the onset of a vacancy diffusion mechanism. Akse et al. earlier came to the same conclusion of a dominant interstitial diffusion mechanism for Ti^{4+} self diffusion in slightly reduced rutile TiO_2,[29] although no similar study has been carried out on SnO_2. Therefore, it is expected that cation interdiffusion occurs in the MBE samples via the interstitial mechanism, although the vacancy mechanism cannot be ruled out, especially in the Sn-rich phase. Fick's second law of diffusion solved for a thin film diffusing into a semi-infinite substrate is[29]

$$c = \frac{\alpha^2}{\sqrt{\pi D t}} \exp\left(\frac{-x^2}{4Dt}\right)$$

where c is the dopant concentration at time t and displacement x from the interface, α is the initial concentration of dopant, and D is the diffusion coefficient. D can be found by plotting $\ln(c)$ against x^2. The relationship between the intensity of a SIMS signal and the material composition can be complex and is frequently non-linear. However, plots of the natural logarithm of the SIMS intensity against the square of the depth contain linear regions (an example given in Figure 5), and this suggests that the SIMS intensity may be a valid linear measure of the dopant concentration in this case.

The diffusion coefficients for diffusion of Ti into SnO_2 (D_{Ti}) and Sn into TiO_2 (D_{Sn}) at the temperatures (500−775 °C) and

Table 1. Diffusion coefficients for Sn in TiO_2 and Ti in SnO_2 estimated from SIMS data.

growth yemperature (°C)	D_{Ti} ($\times 10^{-16}$ cm^2 s^{-1})	D_{Sn} ($\times 10^{-16}$ cm^2 s^{-1})
500	1.8	0.26
600	1.8	1.8
750	47	76
763	31	60

oxygen partial pressure (2×10^{-5} mbar) investigated, can be obtained from the gradients of the plots of the type shown in Figure 5 and are given in table 1. These values are comparable to those previously reported for Sn, Ti, and Zr diffusion in TiO_2 at a variety of temperatures and oxygen partial pressures,[26,29,30] whereas no values have been previously published for D_{Ti}.

Conclusion

In conclusion, MBE has been used to grow films of SnO_2 on rutile TiO_2 (110). Two distinct growth regimes can be identified: firstly growth of a Sn rich film with increasing diffusion and formation of $Ti_xSn_{1-x}O_2$ at increasing T_g, and secondly direct diffusion of the incident Sn ions into the substrate without formation of a Sn-rich layer. This methodology might be useful for studying the functional properties of ideal TiO_2-SnO_2 systems.

Acknowledgment. This work in Oxford was supported by European Union grant NATAMA (NMP3-CT-2006-032583). The NCESS facility at Daresbury Laboratory is supported by EPSRC Grant EP/E025722/1. The authors thank Loughborough Surface Analysis Ltd. for SIMS analysis.

References

(1) Naidu, H. P.; Virkar, A. V. *J. Am. Ceram. Soc.* **1998**, *81*, 2176–2180.
(2) Williams, D. E. *Sens. Actuators, B* **1999**, *57*, 1–16.
(3) Gopel, W.; Schierbaum, K. D. *Sens. Actuators, B* **1995**, *26*, 1–12.
(4) Lin, J.; Yu, J. C.; Lo, D.; Lam, S. K. *J. Catal* **1999**, *183*, 368–372.
(5) Kutty, T. R. N.; Avudaithai, M. *Chem. Phys. Lett.* **1989**, *163*, 93–97.
(6) Vinodgopal, K.; Kamat, P. V. *Environ. Sci. Technol.* **1995**, *29*, 841–845.
(7) Zakrzewska, K.; Radecka, M. *Thin Solid Films* **2007**, *515*, 8332–8338.
(8) Tian, H.; Ma, J. F.; Xie, L. J.; Zhao, Z. Q.; Zhou, J.; Wang, Y. G.; Tao, J. T.; Zhu, X. Y. *Ceram. Int.* **2007**, *33*, 915–918.
(9) Fresno, F.; Guillard, C.; Coronado, J. M.; Chovelon, J. M.; Tudela, D.; Soria, J.; Herrmann, J. M. *J. Photochem. Photobiol., A* **2005**, *173*, 13–20.
(10) Pilkenton, S.; Raftery, D. *Solid State Nucl. Magn. Reson.* **2003**, *24*, 236–253.
(11) Sensato, F. R.; Custodio, R.; Longo, E.; Beltran, A.; Andres, J. *Catal. Today* **2003**, *85*, 145–152.
(12) Kanai, N.; Nuida, T.; Ueta, K.; Hashimoto, K.; Watanabe, T.; Ohsaki, H. *Vacuum* **2004**, *74*, 723–727.
(13) Chambers, S. A. *J. Phys.: Condens. Matter* **2008**, *20*.
(14) Semancik, S.; Cavicchi, R. E. *Thin Solid Films* **1991**, *206*, 81–87.
(15) Wakabayashi, H.; Suzuki, T.; Iwazaki, Y.; Fujimoto, M. *Jpn. J. Appl. Phys., Part 1* **2001**, *40*, 6081–6087.
(16) Caslavsk, V; Roy, R. *J. Appl. Phys.* **1969**, *40*, 3414.
(17) Batzill, M.; Burst, J. M.; Diebold, U. *Thin Solid Films* **2005**, *484*, 132–139.
(18) Batzill, M.; Diebold, U. *Prog. Surf. Sci.* **2005**, *79*, 47–154.
(19) Bertoncello, R.; Casagrande, A.; Casarin, M.; Glisenti, A.; Lanzoni, E.; Mirenghi, L.; Tondello, E. *Surf. Interface Anal.* **1992**, *18*, 525–531.
(20) Takahashi, I.; Payne, D. J.; Palgrave, R. G.; Egdell, R. G. *Chem. Phys. Lett.* **2008**, *454*, 314–317.
(21) Hirata, T.; Ishioka, K.; Kitajima, M.; Doi, H. *Phys. Rev. B* **1996**, *53*, 8442–8448.
(22) Cassia-Santos, M. R.; Souza, A. G.; Soledade, L. E. B.; Varela, J. A.; Longo, E. *J. Thermal Anal. Calorim.* **2005**, *79*, 415–420.
(23) Uchiyama, H.; Imai, H. *Chem. Commun.* **2005**, 6014–6016.
(24) Sayle, D. C.; Catlow, C. R. A.; Perrin, M. A.; Nortier, P. *J. Phys. Chem. Solids* **1995**, *56*, 799–805.
(25) Andersso, Po; Kollberg, E. L.; Jelenski, A. *J. Phys. C: Solid State Physics* **1974**, *7*, 1868–1880.
(26) Sasaki, J.; Peterson, N. L.; Hoshino, K. *J. Phys. Chem. Solids* **1985**, *46*, 1267–1283.
(27) Freeman, C. M.; Catlow, C. R. A. *J. Solid State Chem.* **1990**, *85*, 65–75.
(28) Drobeck, D. L.; Virkar, A. V.; Cohen, R. M. *J. Phys. Chem. Solids* **1990**, *51*, 977–988.
(29) Akse, J. R.; Whitehurst, H. B. *J. Phys. Chem. Solids* **1978**, *39*, 457–465.
(30) Sinclair, W. R.; Loomis, T. C. *Angew. Chem., Int. Ed.* **1958**, *70*, 603.

CG8009404